
Article:

Chinembiri, K., He, S. orcid.org/0000-0003-0326-2447, Li, J. et al. (1 more author) (2019) Numerical study of heat transfer in a distorted rod bundle. Nuclear Engineering and Design, 349. pp. 63-77. ISSN 0029-5493

https://doi.org/10.1016/j.nucengdes.2019.04.003

Numerical study of heat transfer in a distorted rod bundle

Kenneth Chinembiri[a], Shuisheng He[a,*], Jiankang Li[b], Cosimo Trinca[a]

[a] *Heat, Flow and Turbulence Research Group, Department of Mechanical Engineering, The University of Sheffield, S1 3JD, UK*

[b] *Fuel Route Systems Branch, Engineering, EDF Energy Generation, Barnett Way, Barnwood, Gloucester, GL4 3RS, UK*

Abstract

The effect of rod distortion on the flow and heat transfer in a rod (fuel) bundle similar to those in an Advanced Gas-cooled Reactor (AGR) is investigated using carefully constructed CFD models. The results are of relevance to various other engineering applications, for example heat exchangers. The distorted element contracts gradually over the first half of the element, reaching a minimum at half high then subsequently increasing back to its normal value over the second half of the element. In this paper, the results for forced convection are presented. Changes in the rod profiles divert flow to regions of less resistance, resulting in strong cross flow recirculation regions. The resultant three dimensional flow is also accompanied by large scale swirling flow around the fuel pins. The hotspot at any height coincides with the leeward side of the cross flow. It is rather surprising that the peak can temperature at the location of worst bundle distortion(i.e middle height) is actually slightly lower than that of intact fuel. The overall peak can temperature in the damaged bundle is however much higher than that in the intact fuel, and this occurs towards the top of the bundle.

---

1. Introduction

Rod bundles are prevalent in many industrial systems. In particular, most nuclear reactors utilize fuel bundles consisting of cylindrical fuel rods arranged in a geometric array. As the coolant is forced through the rod bundle heat transfer occurs. Understanding the physical mechanisms, which underlie this process is important with regards to maintaining safety. In this study the effect of rod bundle distortion on the flow and heat transfer is investigated for an Advanced Gas-cooled Reactor (AGR) rod bundle. The distortion investigated herein is termed *Wheatsheaf* and can arise if the irradiated rod bundle is dropped during the re-fuelling process. A *Wheatsheaf* bundle is characterised by a reduction in the pitch to diameter (p/d) ratio gradually over the first half of the element, reaching a minimum ($p/d \approx 1.2$) at half high, and then a subsequent increase back to the normal $p/d(\approx 1.8$) ra-

---

[*] s.he@sheffield.ac.uk

Preprint submitted to Nuclear Engineering and Design *April 3, 2019*

tio over the second half of the element (see Fig.1a).

Nomenclature

Superscripts

$*$	quantity normalised using bulk values (unless indicated otherwise)
$+$	quantity normalised using wall scales

Greek letters

δ_{ij}	Kronecker delta
ϵ	dissipation term
μ	molecular viscosity
μ_t	turbulent viscosity
ω	specific dissipation rate
ϕ_{ij}	pressure strain tensor
ρ	density
τ_w	wall shearstress)

Roman Letters

λ	thermal conductivity
C_p	specific heat
C_μ	model specification
d	diameter of fuel rod (m)
k	turbulent kinetic energy
P	production term
p	pitch
p/d	pitch to diameter ratio
S_{ij}	Strain tensor
T	temperature
t	time
T^*	normalised temperature; $\frac{T-T_{inlet}}{T_{b,outlet}-T_{inlet}}$
U	normalised velocity; u/u_b
u	velocity
$u^{'}$	velocity fluctuation
u^*	friction velocity; $\sqrt{\tau_w/\rho}$
u^+	dimensionless velocity; u/u^*
uv	turbulent shear stress
v	kinematic viscosity; μ/ρ
w/d	wall to diameter ratio
y	normal distance from wall
y^+	dimensionless normal distance from the wall

Subscripts

a	axial
b	bulk
i, j, k	directional terms

There are many sources in literature investigating the flow and heat transfer in rod bundles at design conditions. However for rod bundles at non-design conditions there is sparse literature available. Ouma and Tavoularis [1] investigated rod bundles at both design and non-design conditions. In the experimental setup they could displace the middle pin towards the wall or other pins. They found that as the p/d or wall to diameter w/d ratio decreased, shear stress showed significant increase. Also as the gap length decreased there was more pronounced contour bulging. Triangular subchannel asymmetry was investigated by Hofmann [2]. It was found that moderate degrees of asymmetry lead to considerable velocity and temperature changes in the coolant. Heina et al[3] performed isothermal investigations into undamaged and damaged rod bundles. The aforementioned paper is in Russian but a synopsis is given in an IAEA report [4]. Their results showed a decrease in mass flow in the reduced subchannel, which in turn lead to increased temperatures in the respective subchannels. Krivent-sev and Ninokata [5] perfomed a RANS (Reynolds Averaged Navier Stokes) simulation of a rod bundle with a displaced pin. In the reduced gap their p/d ratio was 1.026 compared to the nominal p/d ratio of 1.17.

Their results showed satisfactory agreement to experimental data. Davari et al.[6] simulated channel flow blockage caused by the buckling of fuel plates. The simulation used a realisable $k-\epsilon$ model with advanced wall functions. Various blockage levels were investigated and results showed that the integrity of the cladding was compromised above 50% blockage and nucleate boiling predicted above 70%. Salamana and El-Morshedy [7] simulated buckled flow in a geometry akin to that used Davari et al[6]. Flow blockages of up to 90% were simulated using again the realisable $k-\epsilon$ model. Chauhan et al.[8] studied the effect of displacing the rodbundle towards the pressure tube wall. Their numerical study utilised a $k-\omega$ sst turbulence model. Various degrees of eccentricity were investigated and at maximum eccentricity, turbulent kinetic energy was found to reduce by as much as 63% in the narrow gap of the peripheral subchannel, while a temperature increase of over 200% was noted.

Next, the literature pertaining to general flow features prevalent in rod bundle flow is discussed. Skinner et al[9] conducted an experimental study investigating the rate of heat transfer between subchannels. Results obtained revealed that mixing was higher than what sole turbulent diffusion theory predicted. Increased subchannel mixing measured by Skinner et al was a result of the pulsating flow structure, which was first experimentally determined by Hooper and Rehme[10]. The pulsating flow structure's influence is dependant on the p/d ratio. Krauss and Meyer[11] stated the turbulent kinetic energy and temperature fluctuations at the gap are significant in an array with a p/d ratio of 1.06 compared to that of 1.12. Yan et al [12] performed numerical simulations using tight triangular lattices of varying p/d ratios. In their work it was shown that the critical p/d ratio was 1.06, below and above this p/d ratio the strength of the coherent structure decayed and at a p/d ratio above 1.12 it was considered weak. Interestingly, recent work by Duan and He [13] and Mohd amin et al [14] has shown the strouhal number of this flow structure is geometry dependant even in the event of strong buoyancy influence [13] and strong property variation[14]. Chang and Touvelaris [15, 16] showed that for tight rod bundle lattice's where the pseudo periodic pulsation is non-negligible, the URANS method in conjuction with a RSM returned results in good agreement to those obtained from an experimental setup. Similarly, the review of by Meyer [17] on code application and Sofu et al[18] show for arrays smaller than p/d ratio 1.1 URANS improved the accuracy of predicted results and for arrays with p/d ratios larger than threshold the RANS method provided reasonable solutions. This was particularly the case if the RANS method was used in conjunction with an anisotropic turbulence model. Another flow feature prevalent in rod bundles is secondary flows which arise due to the anisotropy of Reynolds stress[19, 20]. Typically this flow structure is quite small, with an order of magnitude $<1\%$ of bulk velocity. The p/d ratio appears to have an effect on the magnitude, for example, Rapley and Gosman[21] reported higher secondary velocities at lower p/d ratios. Based on the work above and further work by Vonka[22], Carajiscov and Toderas[23], and Rehme[24], the following is revealed about secondary flows in rod bundles. Secondary flows are a flow pattern perpendicular to the predominant flow direction and arise due to the anisotropy of the Reynold's stress. This flow feature redistributes the turbulence inside subchannels and alters the variation of wall shear stress.

Based on the literature discussed above and to the authors best knowledge, no numerical simulations have been conducted on such a distorted AGR bundle. This paper aims to investigate the Wheatsheaf bundle so as to understand the flow phenomena and physics in such a uniquely distorted geometry. Understanding the aforementioned is important with regards to maintaining safety in the unlikely event of dropped/damaged fuel during refuelling procedures.

2. Modelling description

Computations were carried out using the open source CFD solver *Code_Saturne*, which is a general purpose, single-phase solver developed by EDF. The code uses the unstructured finite volume method to solve the Reynolds averaged (or filtered) Navier-Stokes equations and can handle a wide variety of unstructured meshes. All the calculations performed in this work are conducted using the RANS method. To close the RANS formulation of the Navier-Stokes equations a turbulence model has to be used. For this study a number of high Reynolds number turbulence models available in *Code_Saturne* are examined for their impact on the solution. The models investigated are the k-ϵ model, k-ω SST model and SSG Reynolds stress turbulence model. Since there is no detailed experimental data available for the wheatsheaf geometry, a turbulence model comparison was performed by reproducing the experimental work of Trupp and Azad [19], this study is described in Section 3. The k-ϵ model and k-ω SST model are two equation Eddy Viscosity Models(EVM). These models are based on Boussinesq's hypothesis, in which the Reynolds stresses are proportional to the strain rate tensor. For an incompressible flow, the relation is simply:

$$\rho\overline{u_i^{\prime}u_j^{\prime}} = 2\mu_t S_{ij} - \frac{2}{3}k\delta_{ij} \tag{1}$$

To solve for the Reynolds stress component, μ_t is obtained by solving two transport equations, one for turbulent kinetic energy and another for turbulent dissipation rate. The eddy viscosities are defined as follows for k-ϵ and k-ω SST models, respectively.

$$\mu_t = C_\mu \frac{k^2}{\epsilon} \tag{2}$$

$$\mu_t = \frac{a_1 k}{\max(a_1\omega, \Omega F_2)} \tag{3}$$

The transport equations solved for k-ϵ model[25] are detailed below:

$$\frac{\mathrm{D}(\rho k)}{\mathrm{D}t} = \frac{\partial}{\partial x_j}\left[\left(\mu + \frac{\mu_t}{\sigma_k}\right)\frac{\partial k}{\partial x_j}\right] + P_k - \rho\epsilon \tag{4}$$

$$\frac{\mathrm{D}(\rho\epsilon)}{\mathrm{D}t} = \frac{\partial}{\partial x_j}\left[\left(\mu + \frac{\mu_t}{\sigma_\epsilon}\right)\frac{\partial \epsilon}{\partial x_j}\right] + \frac{\epsilon}{k}(C_{\epsilon 1}P_k) - \frac{\epsilon}{k}(C_{\epsilon 2}\rho\epsilon) \tag{5}$$

The k-ω SST[26] combines the standard k-ω and k-ϵ models. The k-ω model is solved near the wall while in remote regions the model transforms to the k-ϵ model. Blending of the two standard models is achieved through the function F. Transport equations solved by the k-ω SST are detailed below:

$$\frac{\mathrm{D}(\rho k)}{\mathrm{D}t} = \frac{\partial}{\partial x_j}\left[(\mu + \mu_t\sigma_k)\frac{\partial k}{\partial x_j}\right] + P_k - \beta^*\rho k\omega \tag{6}$$

$$\begin{aligned}\frac{\mathrm{D}(\rho\omega)}{\mathrm{D}t} = \frac{\partial}{\partial x_j}\left[(\mu + \mu_t\sigma_\omega)\frac{\partial \omega}{\partial x_j}\right] + \alpha\frac{\omega}{k}P_k - \\ \beta\rho\omega^2 + 2\rho(1-F)\frac{\sigma_{\omega 2}}{\omega}\frac{\partial k}{\partial x_j}\frac{\partial \omega}{\partial x_j}\end{aligned} \tag{7}$$

Constants for the k-ϵ model used in the simulations are defined as follows[27]. $C_\mu = 0.009$; $\sigma_k = 1.0$; $\sigma_\epsilon = 1.3$; $C_{\epsilon 1} = 1.44$; $C_{\epsilon 2} = 1.93$; Constants/parameters for the k-ω SST model are defined as follows[27]: $a_1 = 0.31$; $\beta^* = 0.009$; $\Omega = \sqrt{2S_{ij}S_{ij}}$; $F_2 = \tanh\ \max\left(\frac{2\sqrt{k}}{0.009\omega y}, 500\frac{v}{\omega y^2}\right)$; $\sigma_{\omega 1} = 2.0$; $\sigma_{\omega 2} = 1.0/0.856$; $\sigma_{k1} = 1.0$; $\sigma_{k2} = 1.0$; $\beta_1 = 0.075$; $\beta_2 = 0.0828$; $\alpha_1 = \frac{\beta_1}{\beta^*} - \frac{k^2}{\sqrt{\beta^*\sigma_{\omega 1}}}$; $\alpha_2 = \frac{\beta_2}{\beta^*} - \frac{k^2}{\sqrt{\beta^*\sigma_{\omega 2}}}$

The SSG Reynolds stress model[28] is a second order turbulence model, which directly solves the Reynolds stress terms in the RANS equation. As a result this model can capture the anisotropy of turbulent stresses. Individual Reynolds stresses are solved, along with an equation for turbulent dissipation. Below the transport equation for the Reynolds stresses is shown:

$$\begin{aligned}\frac{\mathrm{D}(\overline{u_i^{\prime}u_j^{\prime}})}{\mathrm{D}t} = \frac{\partial}{\partial x_k}\left(v\frac{\partial\overline{u_i^{\prime}u_j^{\prime}}}{\partial x_k}\right) + P_{ij} - \frac{2}{3}\delta_{ij}\epsilon \\ +\phi_{ij}\end{aligned} \tag{8}$$

The modelling of the pressure-strain tensor(ϕ_{ij}) is important, as this term is responsible for transferring energy from the largest normal stress to the smaller normal stresses. This term is modelled using the pressure strain correlation detailed by Speziale and Gatski[28]. Model constants and parameters are as defined by Speziale and Gatski[28].

The thermal energy equation for all simulations presented herein is based on the form for temperature, and assumes the flow is incompressible or weakly compressible:

$$\rho C_p \frac{\mathrm{D}T}{\mathrm{D}t} = \frac{\partial}{\partial x_i}\left[\left(\frac{\mu}{Pr} + \frac{\mu_t}{Pr_t}\right)\frac{\partial T}{\partial x_i}\right] + S \qquad (9)$$

Where S is a volumetric source term and the turbulence heat flux has been modelled using the simple gradient diffusion hypothesis, namely, $\rho\overline{u_i^{'}T'} = \frac{\mu_t}{Pr_t}\left(\frac{\partial T}{\partial x_i}\right)$

Some the results presented in the later sections try to take into account roughness of AGR rodbundles through the use of an effective roughness. To conclude this section roughness wall function model used in *Code_Saturne* is briefly described below, in this equation z_0 is the roughness[27].

$$u^+ = \frac{1}{0.42}\ln\left(\frac{y + z_0}{z_0}\right) + 5.2 \qquad (10)$$

2.1. Wheatsheaf case description and methodology

A schematic of the modelled geometry can be seen in Fig.1. The modelled geometry consists of two sections. At the bottom is a 0.3 m tall undamaged section, where the flow is mapped back to the inlet at half high. By mapping the downstream values to the inlet it is possible to obtain a fully developed profile. The second section is joined to this development section by conformal joining. As mentioned earlier, this section consists of a 1 m tall *Wheatsheaf* rod bundle. Coolant flowing through the bundle is forced through the pin gaps (interstices in the array), which are commonly referred to as subchannels. AGR fuel bundles have an azimuthally repeating pattern, of which a 30° sector is chosen to be the computational domain(Fig.1c). At the inlet of the computational domain a uniform inlet velocity boundary condition, with a streamwise value of 4.36 m/s is prescribed, giving a mass flow of 3 kg/s into the bundle. The inlet temperature of the flow is set to 300°C. For the outlet, an outflow boundary condition is applied. On the azimuthal faces a symmetry boundary condition is used. It is worth noting as the pins are staggered a rotational periodicity boundary condition is not applicable for a 30° sector. Since this simulation is concerned with the thermal hydraulics of an AGR (Advanced Gas Reactor) stringer during refuelling, following conditions are given. The external boundary wall (sleeve) and central rod wall (guidetube) are treated as adiabatic smooth walls. For the pin walls a constant heat flux of 2.9 kWm^{-2} is applied, in comparison during normal operation the typical heat flux is $\approx 342kWm^{-2}$. A reduced heat flux (in comparison normal operating conditions) is used as the distorted bundle can arise if the fuel stringer is damaged or dropped during refuelling operations. The refuelling scenario modelled for this study assumes offload pressurised refuelling. This would entail that although still pressurised the reactor has

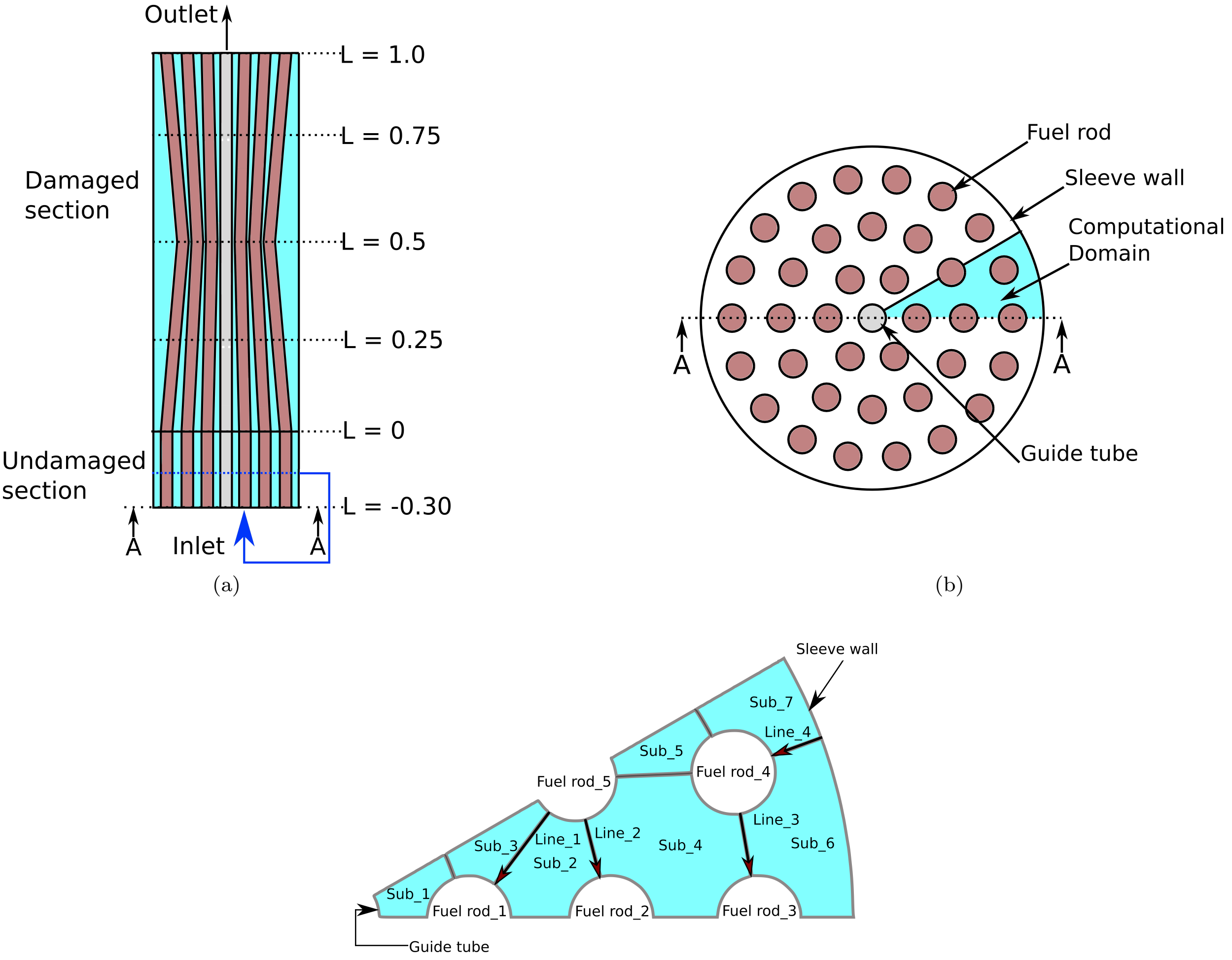

(a) (b)

(c)

Fig. 1: Modelled domain and cross sectional schematic for full and partial subchannel divisions. (a) Internal view along the plane A-A. L is dimensionless height (b) Top view of an AGR rodbundle (c) Schematic showing cross sectional divisions of computational domain (30°)

been shutdown . Pin surfaces are treated as either rough or smooth wall depending on the case. Carbon dioxide at a pressure of 3.5 Mpa is the working fluid. The Reynolds number is 201675 and fluid properties are assumed to be constant. The fluid properties are defined as shown in Table 1

Table 1: Fluid properties defined in the simulations carried out

Property	Value	Unit
ρ	32.72	kg/m^3
μ	2.668x10^{-5}	Pa.s
λ	0.03947	W/m/K
C_p	1093.5	J/Kg/K

When a high Reynolds number (HRN) turbulence model is used, the first node next to the cell must be significantly large, $y^+ = 30$. It is difficult to comply with this requirement for the strongly distorted rod bundle studied here. To rectify this, a scalable wall function has been used which allows the first near-wall node to be at the lower range of the log-law $\approx y^+ = 11$. The approach used is based on limiting the minimum value of y^+ in the fine mesh regions to the minimum of the log-law. In the damaged section the mesh comprises of tetrahedral elements, of near unity aspect ratio, with several prism element layers close to the wall. The undamaged development section comprises of prismatic elements and hexahedral elements near the wall. At the outlet of the domain there are layers of extruded prismatic and hexahedral cells. Momentum and turbulent quantities transport equations are discretised using the second order accurate SOLU (Second Order Linear Upwind) scheme.

3. Results

3.1. Validation

The experimental work of flow in a rod bundle by Trupp and Azad [19] is used to validate the two meshing methods employed for the damaged and undamaged section. For this validation exercise a triangular array with a p/d ratio of 1.35 was selected and flow was specified at a Reynolds number of 59 880. Fig.2 shows a sketch of the geometry. The domain was simulated using periodicity, with the top and bottom faces forming the periodic pair. Pin walls are prescribed as smooth, with a no slip wall boundary condition. Surfaces adjoining the pin walls are given a symmetric boundary condition.

Data used for the validation comparison is extracted along the line Y shown in the figure and compared against experimental data. Simulations have been carried out to (i) test mesh resolution requirement/sensitivity, (ii) effect of using different types of meshes (structured/unstructured) and (iii) performance of different turbulence models. Table 2 shows the configuration of meshes and y^+ values.

Dimensionless values shown in the figures are defined as follows: $k^+ = \frac{k}{u^{*2}}$, $uv^+ = \frac{uv}{u^{*2}}$, $U = \frac{u_a}{u_b}$, where u^* is friction velocity calculated using the cross section averaged wall shearstress, uv is turbulent shear stress, u_b is the bulk velocity and u_a is the streamwise velocity. Fig.3 shows a mesh dependence study based on the normalised velocity and turbulent shear stress. In this mesh dependence study all the meshes compared used a prismatic grid and comparisons were limited to high Reynolds number turbulence models. It can be noted meshes M-TA-3 and M-TA-4 return identical profiles for both quantities. Interestingly, mesh M-TA-1 predicts a discontinuous velocity profile, along with a turbulent shear stress profile with non-uniformities, perhaps as a result of discretization errors. The study further shows that grid independence is achieved much sooner for velocity than for turbulent shear stress. It can be concluded mesh M-TA-3 is sufficiently independent of the grid, the

Table 2: Configuration of meshes used for the triangular array validation study.

Mesh	No cells	Boundary mesh	Core mesh	y^+ values
M-TA-1	710	HEXA	PRISM	11.14
M-TA-2	1590	HEXA	PRISM	11.67
M-TA-3	4224	HEXA	PRISM	11.18
M-TA-4	6612	HEXA	PRISM	11.94
M-TET	16555	PRISM	TETRA	12.17

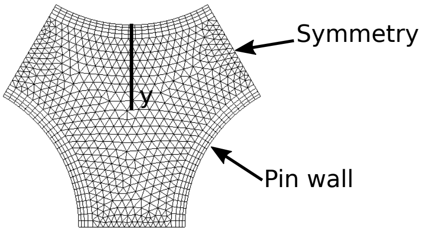

Fig. 2: Slice of prismatic grid(M-TA-3)

cross sectional resolution of mesh M-TA-3 is shown in Fig.2.

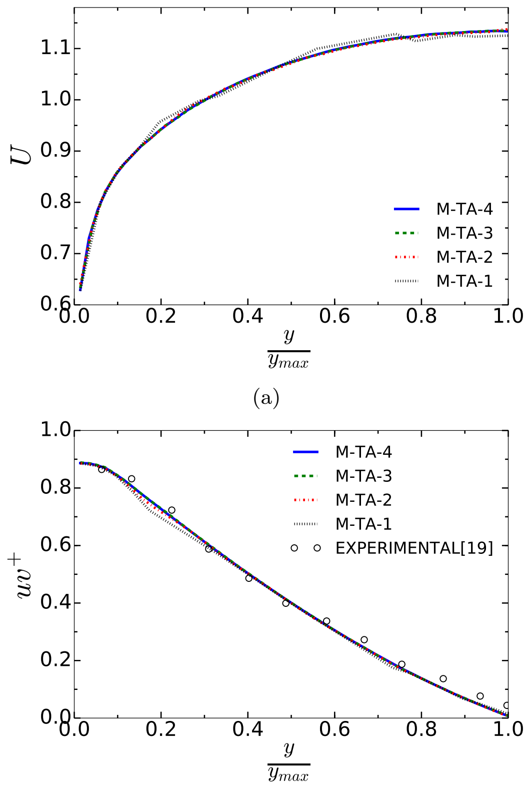

(a)

(b)

Fig. 3: Mesh dependance study (a) Velocity (b) turbulent shearstress

Experience suggests that an unstructured grid based on a tetrahedral mesh needs a density approximately four times greater than that of a structured mesh, and hence an unstructured mesh of four times of that of mesh M-TA-3 is built and used. It should be noted for the tetrahedral mesh there is a single extruded layer at either end of the periodic pair. The extruded layer is required to provide orthogonal cells at the periodic pair upon which a source term is applied to drive the flow.

Fig.4a shows the predicted turbulent kinetic energy from the three turbulence models and the respective grid types. Overall, all simulations have achieved reasonably good agreement with the experiment. Small differences with respect to grid type are observed near the wall and as the grid transitions from the prism layer to the tetrahedral layer. This is evidenced in the slightly different slopes within this region($\frac{y}{y_{max}} \approx 0.2$). With regards to turbulence model performance, the RSM model predicted results somewhat closer to experimental while the eddy viscosity models over predict turbulent kinetic energy levels. For eddy viscosity models the most important parameter is uv which is mostly dependant on the eddy viscosity. Fig.4b shows, turbulent shear stress levels predicted are the same within the bulk region and there are some differences between the results of the various models near the wall. Eddy viscosity models show a marginal over prediction of uv^+ near $\frac{y}{y_{max}} = 0.1$.

Finally, in Fig.4c the dimensionless axial velocity profiles show slight differences between the respective turbulence models and identical profiles in relation to the respective mesh types. The following can be noted based on this brief comparison. Firstly, Reynolds stress model predicted results that best matched experimental data, while eddy viscosity models in particular the $k-\epsilon$ model returned reasonable results. A comparison of different mesh types employed in the validation case showed minute differences. To study flow and heat transfer in the damaged geometry two turbulence models have been selected, for further study these are the $k-\epsilon$ and SSG Reynolds stress model's. The $k-\epsilon$ model has been selected in addition to the SSG model because for an unstructured mesh, the model is more stable, less computationally expensive and less susceptible to local mesh quality deterioration than the RSM model.

3.2. *Mesh dependence and turbulence model comparison Wheatsheaf geometry*

Mesh parameters used in the validation case are applied to the Wheatsheaf case and in particular the wall resolution is maintained, this is achieved through limiting the maximum element surface area. The resulting mesh had a density of 21.5 million in the damaged section(see Fig.5). This resolution was used for all the cases described herein. An additional mesh independence test has been carried out for the damaged fuel section, as the recycling domain has been confirmed mesh independent based on the validation test case. The mesh was coarsened by relaxing the restriction on maximum element area on the pin walls as well as increasing the growth rate (the rate at which tetrahedral cells increase in size from the boundary). Thus only the damaged section is altered and the recycling domain is kept constant thereby resulting in a coarse damaged section of density 15.27 million cells. The mesh configurations used in this dependence study are shown in Table 3. Fig.6 shows the comparison for the normalised turbulent kinetic energy obtained from the Reynolds stress model.

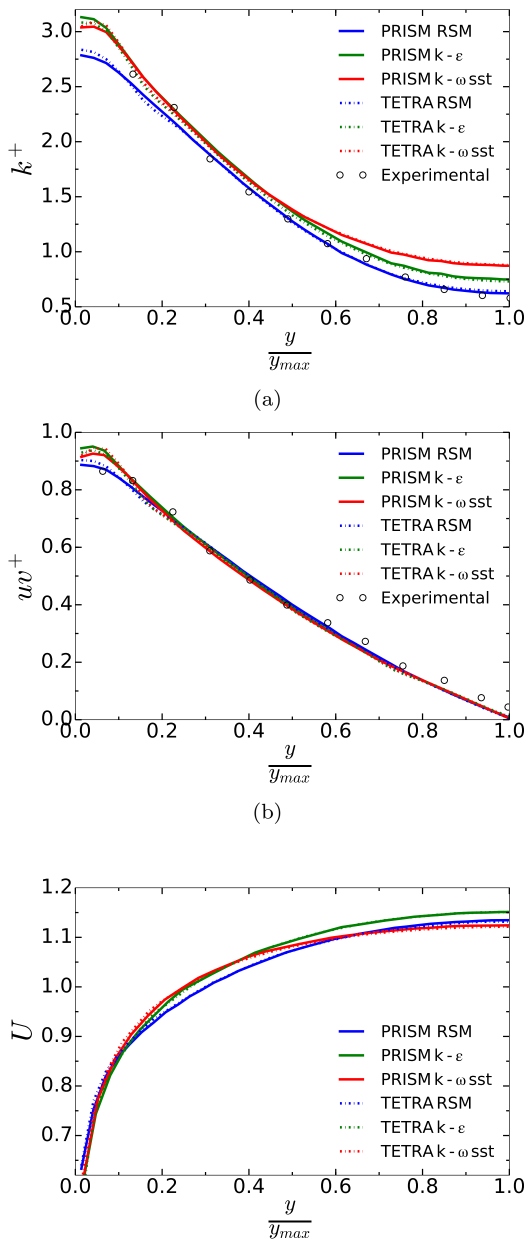

(a)

(b)

(c)

Fig. 4: Study of mesh type and performance of turbulence model (a) Turbulent kinetic energy (b) Turbulent shear stress (c) Velocity

The normalisation for turbulent kinetic energy k^* is defined as k/u_b^2. The RSM model is used to assess mesh independence as it is most susceptible to changes in mesh density. Profiles are obtained from

Table 3: Configuration of meshes used for the triangular array validation study.

Mesh	No cells (10^6)	Boundary mesh	Core mesh	y^+ values
M-1	15.27	PRISM	TETRA	22.87
M-2	21.5	PRISM	TETRA	22.8

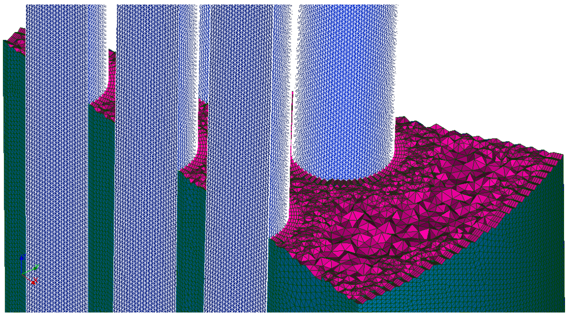

Fig. 5: Clipping of Wheatsheaf mesh

Line_1 (see Fig.1c), at several axial locations. The results are shown to be mesh independent.

A comparison of predicted results obtained from the two turbulence models is given by comparing profiles obtained along Line_1. Fig.7 shows the normalised profiles for temperature, axial velocity and uv. The two turbulence models predict similar trends for all quantities. For the temperature profiles(see Fig.7a), it is interesting to note that initially at the lower axial locations L = 0.25 and 0.5, the differences are relatively small with the maximum difference occurring near rod_1. At L = 0.75 and 1.0 the maximum difference occurs near rod_5, which is now a recirculation zone (further description given later). Furthermore this difference is appreciably larger than that observed at the lower axial locations. The near wall cell temperature values at $y/y_{max} = 0$ for L = 0.75 and 1.0 differ by 1.64 °C and 1.55 °C. Calculating the percentage difference as a function of maximum fluid temperature, the resulting temperature difference is ≈18% and ≈17% respectively.

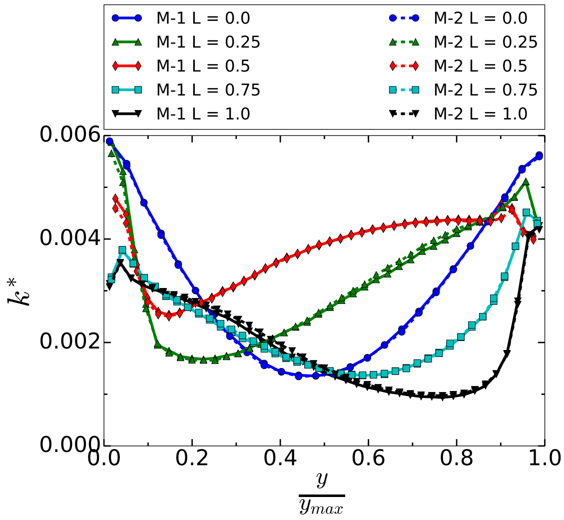

Fig. 6: Mesh dependance study across Line_1

For the normalised velocity, the two models return near identical profiles at the inlet into the damaged section L = 0.0. At higher axial locations some differences occur near the recirculation zones and/or the pin wall. Taking the profile at L = 0.5 and calculating the percentage difference along the profile, the maximum is found to be 3.7 %. Turbulent shear stress profiles show that there is a good agreement between the turbulence models. This is particularly true on the pin surfaces and local regions where the coolant is pushed against the surface. In the recirculation zones, there is an increased difference.

In conclusion it is noted that the two models predict similar trends for the quantities shown and within the recirculation zone differences in the overall values are especially noted. Data presented from hereon will be based on the $k-\epsilon$ model.

3.3. Overall flow pattern and temperature distribution in smooth pin Wheatsheaf results

As mentioned earlier results presented from this point onwards are from the standard $k-\epsilon$ model. Fig.8 the normalised velocity field obtained at different axial locations is shown. At L = 0.0, the local maxima occurs in the subchannel centres. The flow distribution at this height is akin to that obtained from the undamaged bundle. As the rods converge (L = 0.25) the maxima denoted by X shifts towards the outer region. At L = 0.5, the rods are at maximum distortion, with the maxima now fully located in the outer wall subchannel. Furthermore, within this convergent section (up to L = 0.5), high axial velocity regions form in-between the pin gaps.

As the rods diverge back to nominal p/d ratio at L = 0.75, the maxima shifts towards the interior. An interesting observation is the delay in flow redistribution to the changes is rod profile. This can be seen by noting the different contours at L = 0.25 and L = 0.75, where the rod positions are the same. Finally, at L = 1.0 the rods are now back to nominal p/d ratio and as can be seen, the maxima is located in-between the rod gaps and the flow redistribution is clearly significantly different from that at L = 0.0, showing a strong delay. Additional low velocity subregions form on the leeward pin faces(oriented against the shift of local maxima

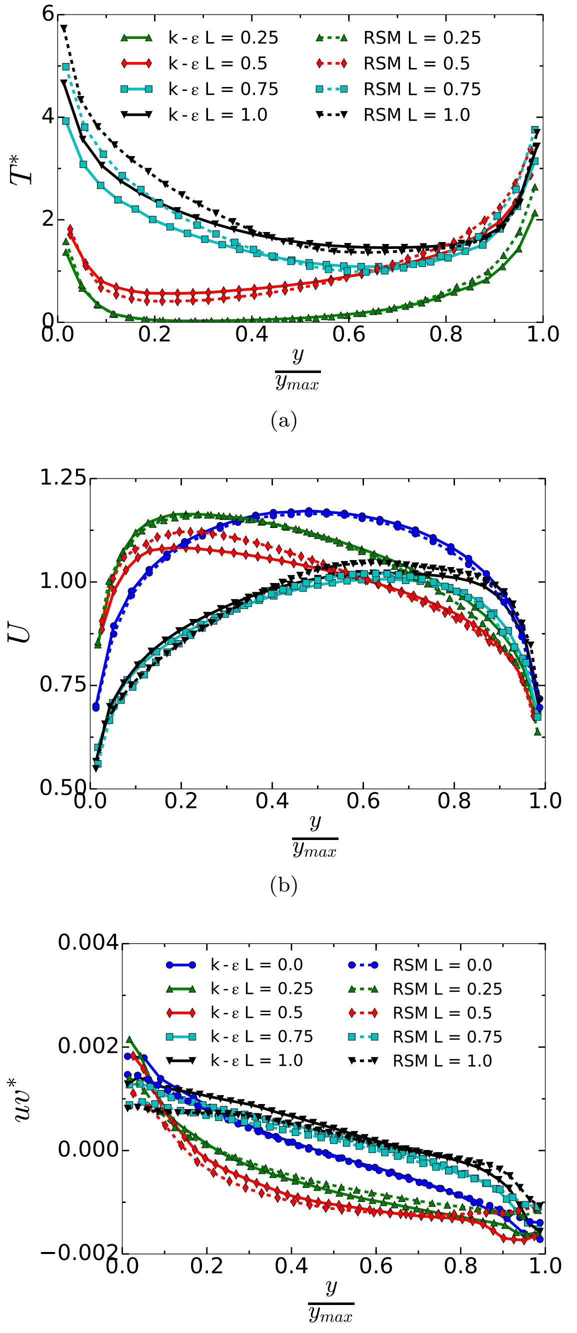

(a)

(b)

(c)

Fig. 7: Comparison between of predictions between $k-\epsilon$ and RSM turbulence models. Distributions along Line_1 of (a) temperature, (b) velocity and (c) turbulent shear stress. (b) and (c) share the same legend.

X). This is true in both converging and diverging sections.

Vector plots of cross flow velocity are presented in Fig.9. The vectors are coloured by the magnitude, which is dimensional and has units of m/s. Due to pin inclination, the subchannel flow is re-disturbed and driven around the fuel pins. This is evidenced by the vectors starting and oriented away from the pin surface, which appear as a mass "source" in a 2D plot. As the flow is driven around the fuel pin, detachment of the cross velocities occurs and recirculation zones form behind the pins. In the wake region, at the rear of the fuel pin, some of the flow is driven towards the pin surface which appears to be a mass "sink" in a 2D plot. The aforementioned behaviour is evident in each of the contour plots shown and the orientation of "sources" and "sinks" alternates depending on the pin inclination. Flow redirection is clearly seen and the cross flow velocities can have magnitudes upto 12.1% of bulk velocity. The magnitudes are especially high in the convergent section and in-between the pin gaps. A strong flow delay is noted at L = 0.5 (location of maximum distortion) where the cross flow is still directed outwards. The delayed reaction of velocity distribution observed is likely to be caused by the inertia of the outward crossflow as after pin inclination alters, the outward flow must be arrested and then redirected towards the interior. To show the three dimensional flow, Fig.10 shows the traces of massless particles released at the inlet of the damaged section. It can be seen clearly that fluid particles swirl around the fuel pins. The direction of the swirl reverses as the fuel changes from converging to diverging. The outward crossflow shown in Fig.9 as the pins contract to the center of the bundle is anticipated. The strong swirl flow is however not all that intuitive. This does have strong implications in the mixing of the fluid and the distribution of temperature.

An overview of turbulent kinetic energy (k) inside the domain is given by contours shown in Fig.11. Generally it can be seen on the leeward rod faces, there are regions of low turbulent kinetic energy, especially in the narrow wake where "sinks" are evident(see Fig.9). In contrast, the windward facing pin surfaces extending upto the location of cross flow velocity detachment have high turbulent kinetic energy values. Similarly, recirculation zones show high turbulence levels.

Cross-sectional pressure contour plots are presented in Fig.12. In the convergent section higher pressures occur within the interior subchannels thus driving the flow from this region. At L = 0.25 and 0.75 a low pressure zone is clearly evident in the gaps between the third rank pins. As the flow can only escape the subchannels through the pin gaps, this leads to induced acceleration and thus in-turn to a lower pressure within this gap region. A reversal of the pressure field occurs when L = 0.5, as the pressure is now lower within the interior. Furthermore, it is noted at locations of sudden change in

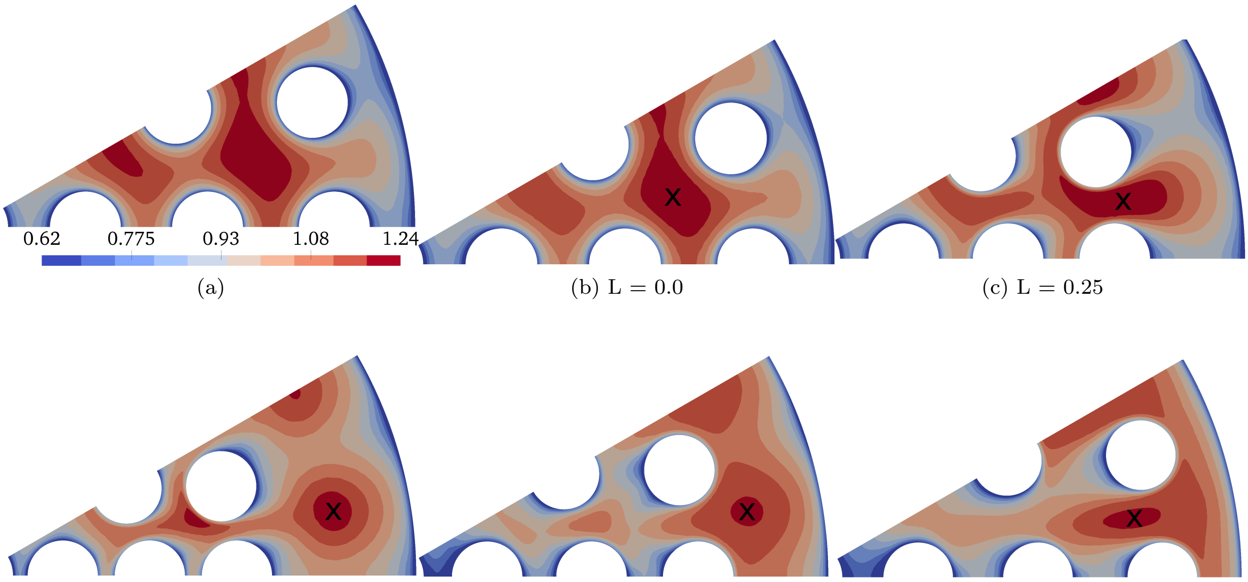

(a) (b) L = 0.0 (c) L = 0.25

(d) L = 0.5 (e) L = 0.75 (f) L = 1.0

Fig. 8: Contours of normalised axial velocity; (a) undamaged bundle and (b - f) from Wheatsheaf bundle.

inclination (L = 0.0, 0.5, 1.0) there is a larger range of pressure, the largest of which occurs at L = 0.5. Such increases in the span are probably the result of stagnation points shifting and reforming. For example at L = 0.5, the forward stagnation point alters by 180° leading to a significant increase in pressure.

Results from the thermal field are presented next. Heating is only applied in the damaged section thus results are shown starting at L = 0.25. Fig.13 shows the normalised temperature distribution at varying heights. In the plots normalised temperature is defined as $T^* = (T - T_{inlet})/(T_{b,outlet} - T_{inlet})$. Lower fluid temperatures are especially evident in the region between the outer rank and adiabatic sleeve wall. Temperature peaks (hotspots) develop on the leeward pin faces. These hotspots seem to coincide with the crossflow velocity detachment points. In contrast, on the windward faces the coolant is pushed against the fuel pin thus enhancing cooling within this subregion of the wall. Furthermore it is interesting that the temperature of the pin at the smallest gap is rather low for example in rod 4 and rod 3. This is clearly due to the strong cross flow.

3.4. Smooth pin quantitative results:

To substantiate the results presented in the contour plots, profiles along several lines (see Fig.1c, arrowed lines on domain show extraction locations) are given for k, velocity and temperature. Velocity profiles are presented in Fig.14. At the inlet of the damaged section, the profiles are largely symmetric. With an increase in height the velocity profile alters considerably. An apex in the velocity profile develops on the windward facing pin. Furthermore,

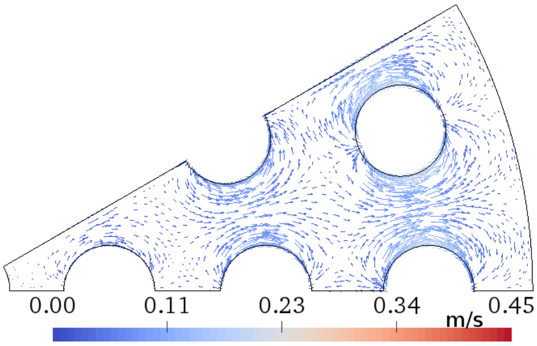

(a) L = 0.0

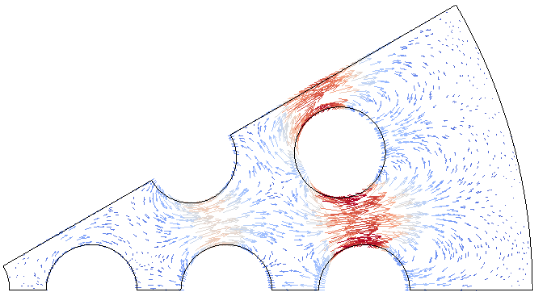

(b) L = 0.25

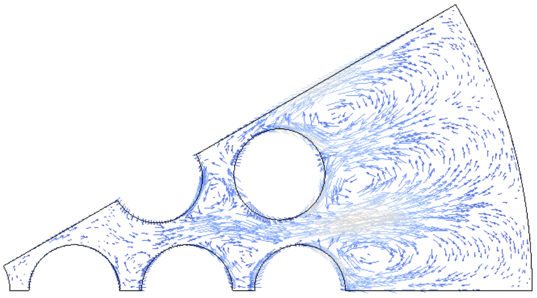

(c) L = 0.5

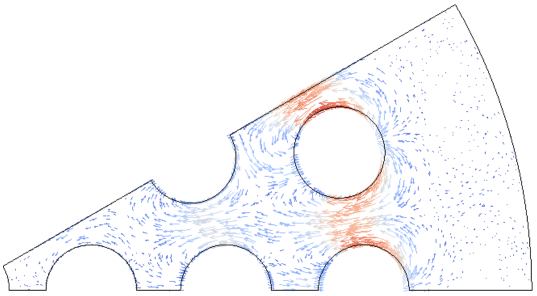

(d) L = 0.75

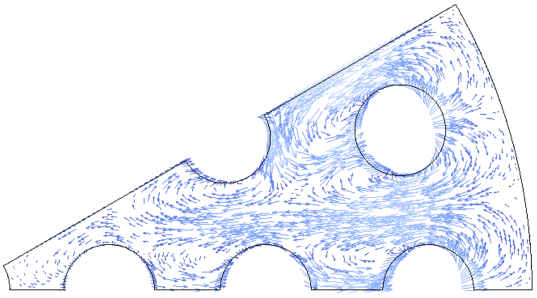

(e) L = 1.0

Fig. 9: Cross sectional velocity vectors. Scalebar is in m/s.

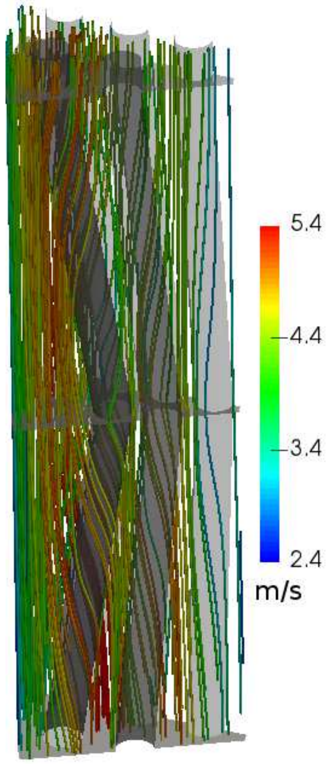

(a)

Fig. 10: 3D Flow streamlines in simulated domain. Different color preset and angle used to allow for easier visualisation

excluding the profile obtained at L = 0.0, peak axial velocity is in the vicinity of the windward pins as the flow accelerates towards these regions. At the pin gap within the second rank, barring the profile at entry, the axial velocity reduces through the domain. In contrast the profile within the gap for the third rank which shows a decrease from L = 0.25 to L = 0.5, before increasing for the later two upper locations. Profiles at these gaps further highlight the strong delay in flow redistribution, as the maxima identified in the contours is yet to fully traverse back towards the interior, as denoted by the still falling axial velocity in pin rank_2. Line_4 reveals an almost monotonic increase of of axial velocity as a function of height.

For k (see Fig.15), profiles across Line_1 exhibit significant variation as the flow develops through the domain. At L = 0.0 the profile is symmetric and as height increases, within the convergent section, peak turbulence levels are observed on fuel_rod 5 which is windward facing. On the opposite pin which is leeward facing there is much lower k.After L = 0.5, the profile reverses shape as crossflow redirection alters. Profiles across the pin gaps are shown in Fig.15b and 15c. Similar to the profile obtained for line_1, peak k levels are located in the convergent section. Asymmetry in some of the profiles is evident and these asymmetries appear to arise due the effect of the far field pin impending on the cross flow. In the subchannel adjacent the sleeve wall (Line_4) there is an overall increase of

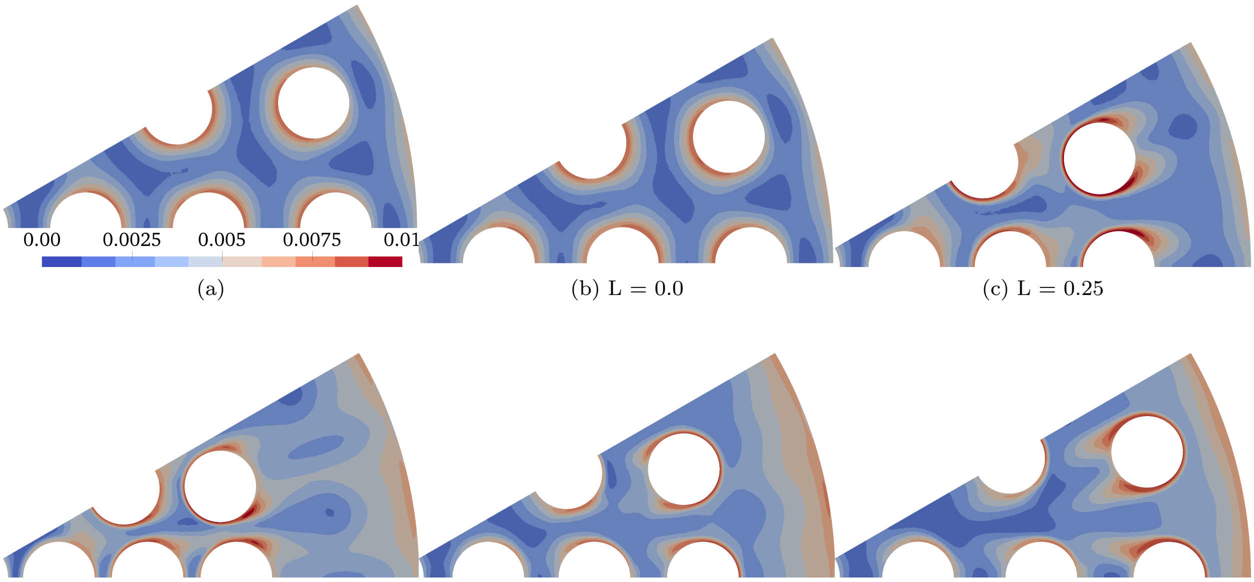

(a)

(b) L = 0.0

(c) L = 0.25

(d) L = 0.5

(e) L = 0.75

(f) L = 1.0

Fig. 11: Contour of normalised kinetic energy; (a) undamaged bundle and (b - f) Wheatsheaf bundle.

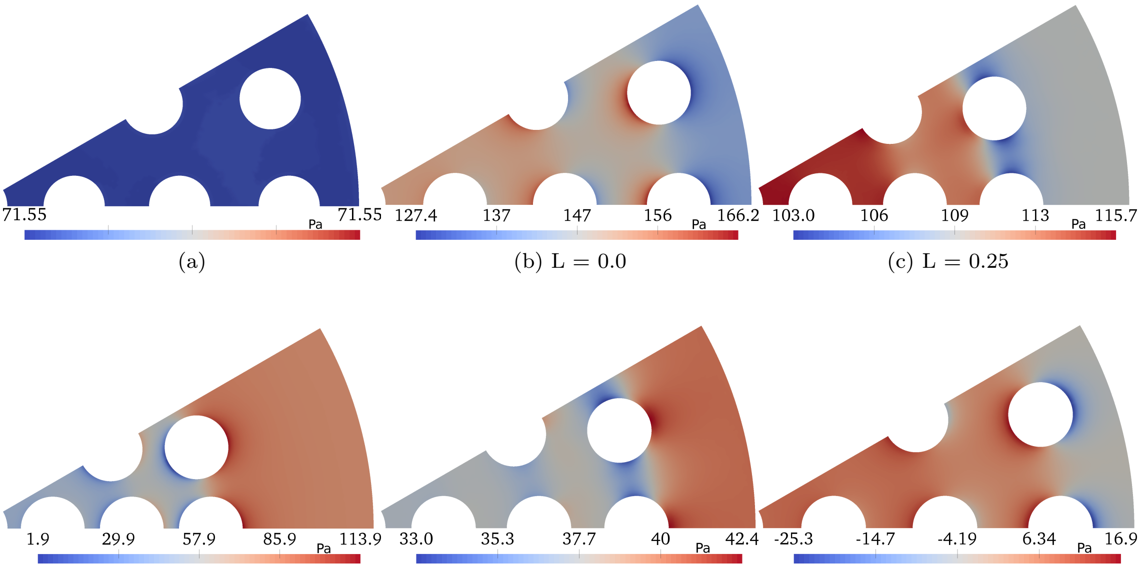

(a)

(b) L = 0.0

(c) L = 0.25

(d) L = 0.5

(e) L = 0.75

(f) L = 1.0

Fig. 12: Contour of pressure; (a) undamaged bundle and (b - f) Wheatsheaf bundle. Scalebar is in Pa.

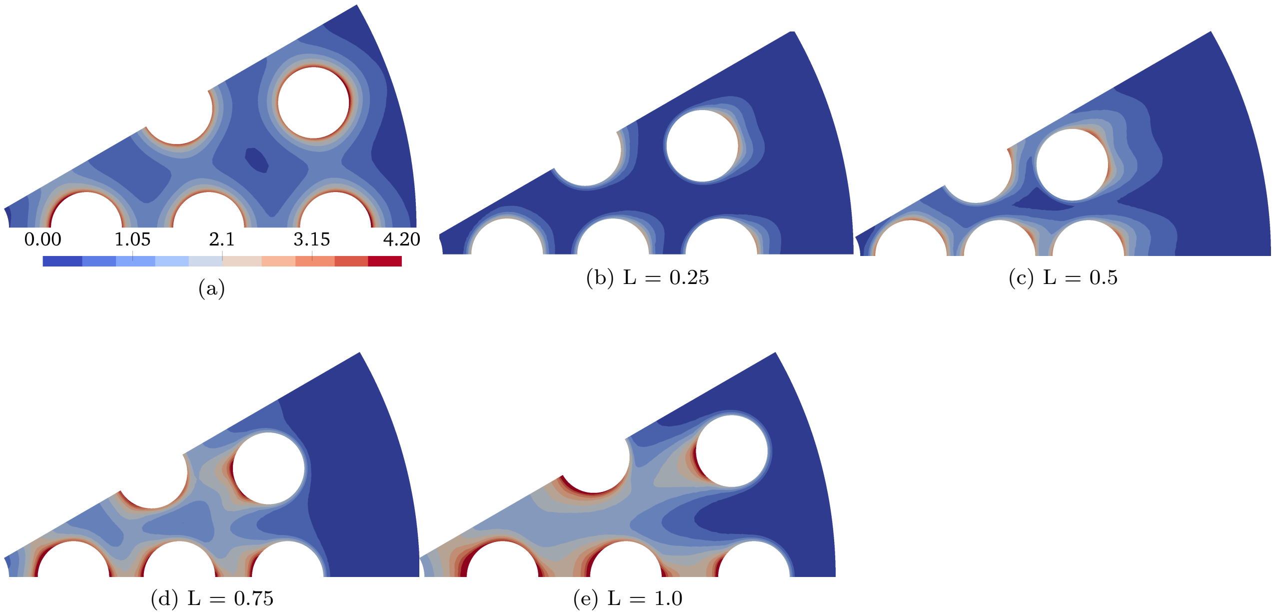

(a)

(b) L = 0.25

(c) L = 0.5

(d) L = 0.75

(e) L = 1.0

Fig. 13: Contour of normalised temperature; (a) undamaged bundle and (b - f) Wheatsheaf bundle.

k within the bulk as a function of height. In contrast to profiles obtained previously peak turbulent kinetic energy occurs in the divergent section.

The temperature profiles in Fig.16 at Line_1 show high temperatures occurring near the pin in the leeward direction(hence weaker convection), with the peak can temperatures occurring at L = 1.0. Line_1 has the highest temperature values compared to other profile extraction lines. The profiles across the second rank pin gap show a monotonic increase in temperature, with the peak temperatures occurring at L = 1.0. Those across the third rank gap interestingly show peak temperatures at L = 0.75, and at L = 1.0 there is an appreciable drop in temperature. This behaviour can be attributed to the increase in axial velocity observed in Fig.14. At L = 0.5, the influence of the far field pins on asymmetry of the temperature profile is apparent. In the outer subchannel however, the peak temperature occurs at L = 0.5, which is the location of maximum distortion.

To help illustrate the differences between rod wall temperature in an undamaged and damaged scenario temperature variations at several heights for pin 4 and pin 1 are plotted respectively, in Fig.17 and 18. For the undamaged bundle, the temperature distribution shows some non-uniformity, but this is relatively small. The peak temperature increases steadily with height. For the distorted bundle, the temperature distributions are significantly altered. The worst peak can temperature is not when the fuel pin is at its most distorted (L = 0.5) but is when the distortion has recovered (L = 0.75 for pin 4 and L = 1.0 for pin 1). The peak can

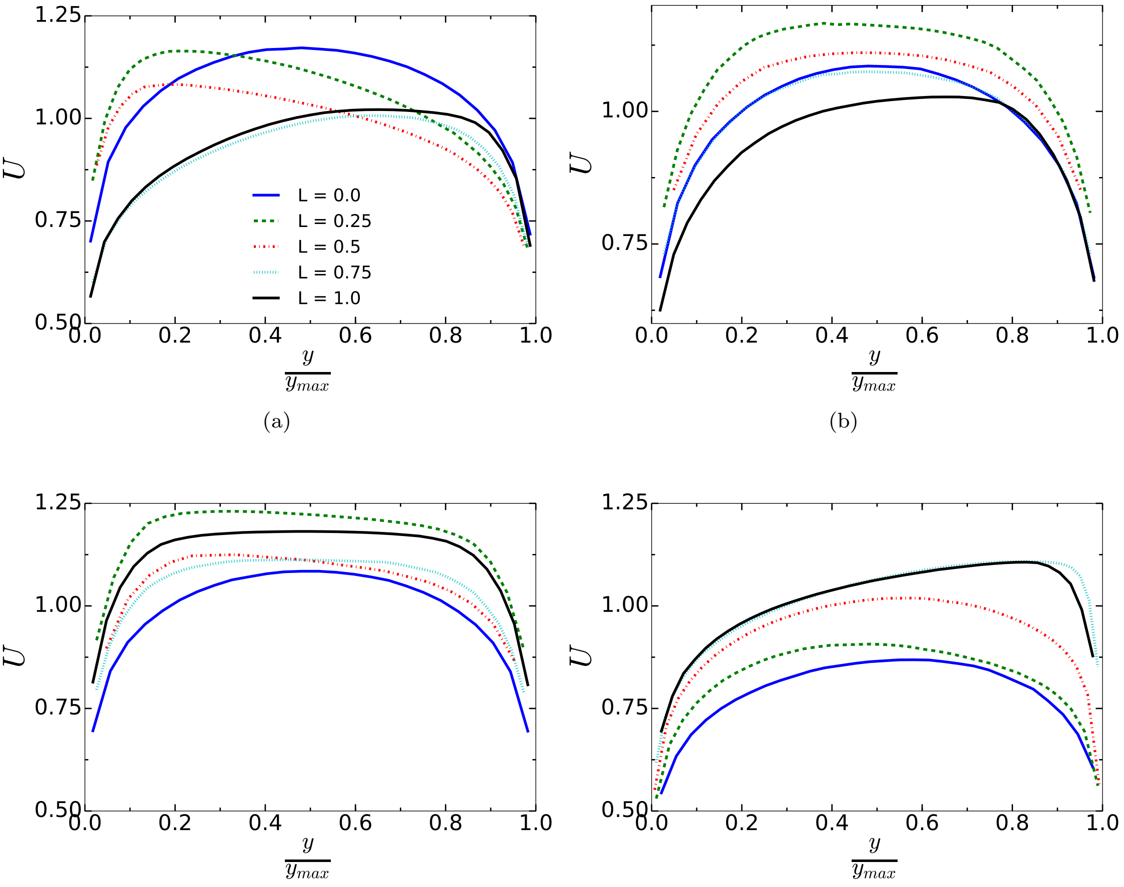

(a)

(b)

(c)

(d)

Fig. 14: Profiles of normalised axial velocity along (a) Line_1, (b) Line_2, (c) Line_3, (d) Line_4

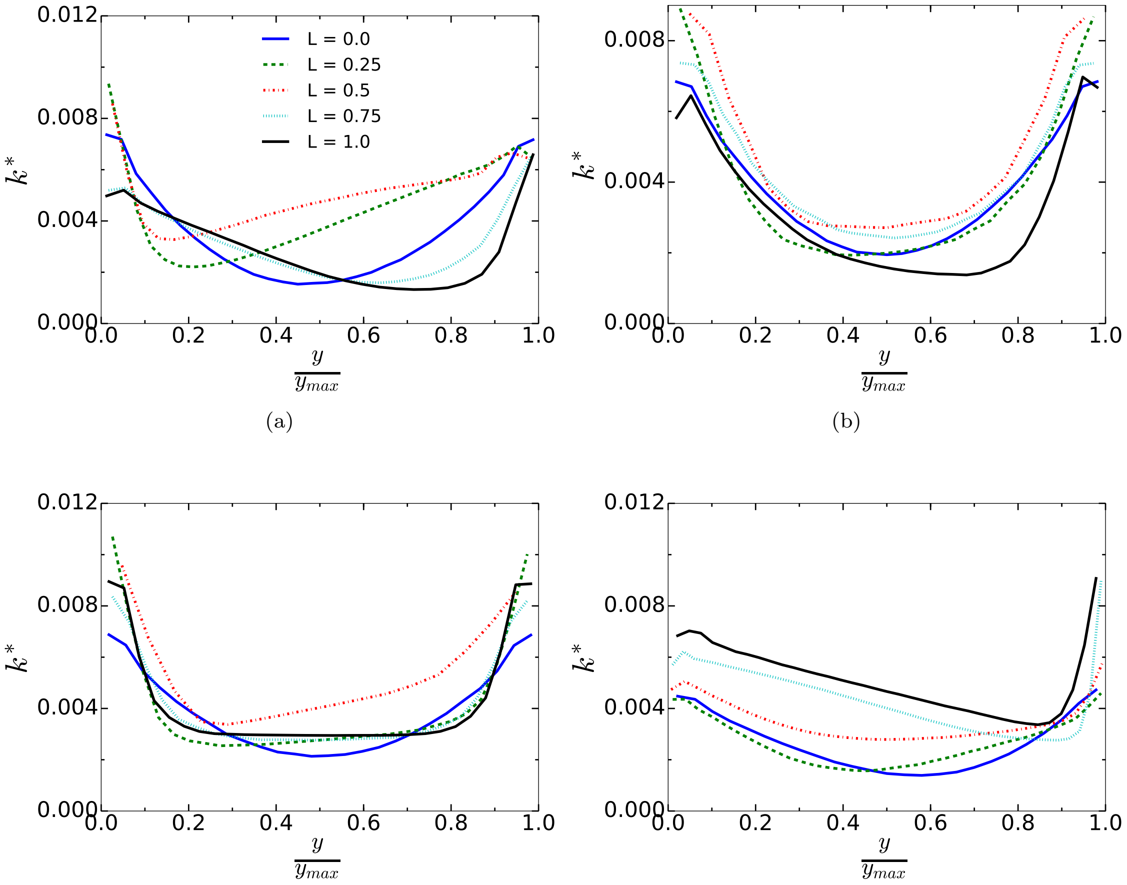

(a) (b)

(c) (d)

Fig. 15: Profiles of turbulent kinetic energy along (a) Line_1, (b) Line_2, (c) Line_3, (d) Line_4

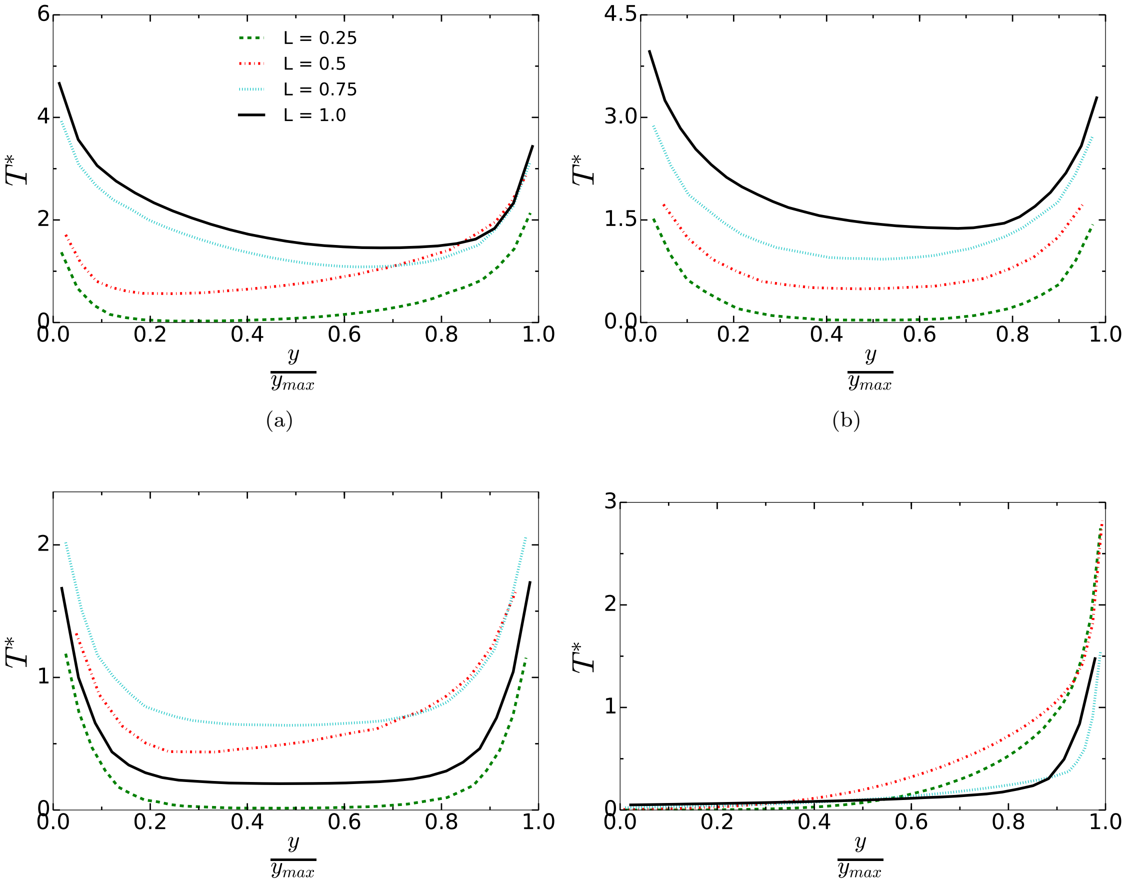

(a)

(b)

(c)

(d)

Fig. 16: Profiles of normalised temperature along (a) Line_1, (b) Line_2, (c) Line_3, (d) Line_4

temperature increases appreciably in the damaged bundle.

Fig. 19 shows the distribution of mass flow in the various subchannels for the damaged and undamaged cases. These profiles are calculated based on the full and partial subchannels present within the 30° sector, the full subchannels are numbered 2, 4 and 6 with the rest being partial (see Fig. 1c). As can be seen for the damaged section, the mass flow for the interior areas reduces in the bottom half and increases in the top section of the geometry. This can be compared to undamaged bundle, which shows no changes in mass flow. It is most interesting to see that the mass flow rate (or bulk velocity) in the various subchannels show a largely symmetric distribution above and between the location of minimum p/d ratio. For example the flow rates at L = 0.25 and L = 0.75. That is the mass flow rate in a subchannel is largely proportional to subchannel areas. This contrasts the observations of the distribution of velocity within each subchannel shown in Fig. 8. The distribution at L = 0.25 and L = 0.75 are very different as discussed earlier. The axial variation of bulk fluid temperature profiles for the undamaged bundle shown in Fig. 20 is linear as expected for a system with a constant heat flux. In comparison, the variations of temperature within the damaged section, are strongly nonmonotonic and complex. This is due to the mixing occurring across the subchannels as a result of the cross flow, as well as the variation of mass flow rate in each subchannel. All the developments for the interior subchannels in the bottom half of the damaged section have a higher rate of temperature increase compared to the peripheral subchannels. In the top half section, the temperature variation alters, for example the subchannels inbetween the second and third rank (numbered 4, 5) show temperature decreases, as to be expected as they have cooler flow arriving from the outer/wall subchannels. The rest of the interior subchannel. nels (numbered 1, 2, 3) show temperature increase. The most surprising result is the slight decrease in temperature for some subchannels (numbered 6, 7). In general, the triangular subchannels have higher coolant temperatures for both undamaged and damaged scenarios. It is noted that the differences between the temperature in the various subchannels are significantly increased in the distorted channel.

4. Simulation with rough fuel pins

In this subsection the effect of rough pins is considered. This is achieved through the use of a wall function and an effective roughness. The value used for effective roughness is based on dividing the average rib height, which for the pins is 0.419 mm, by a constant 3.36. He[29] showed that a value of 3.36 can be used to calculate the effective roughness for rib roughed surfaces. The resulting effective roughness (0.000124) is further evaluated by comparing the pressure drop from a developed flow over a meter tall subchannel at various Reynolds numbers

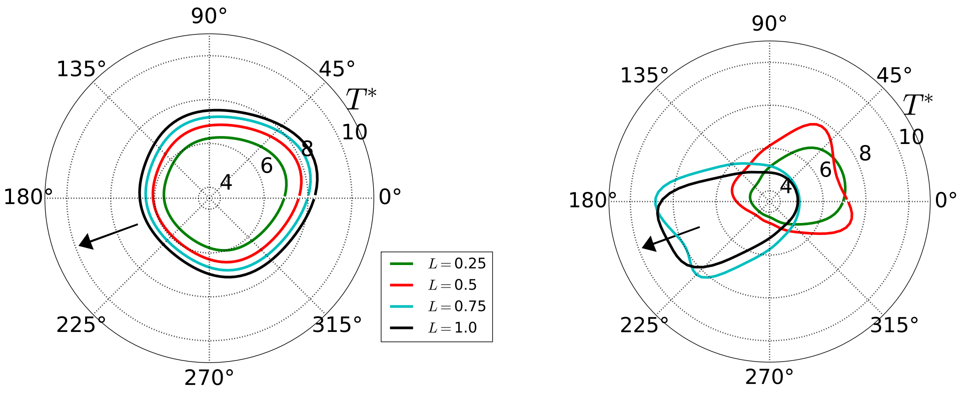

(a) (b)

Fig. 17: Circumferential variation of pin temperature for pin 4. The black arrow at 200° is oriented to the rod bundle center. (a) undamaged bundle (b) *Wheatsheaf* bundle

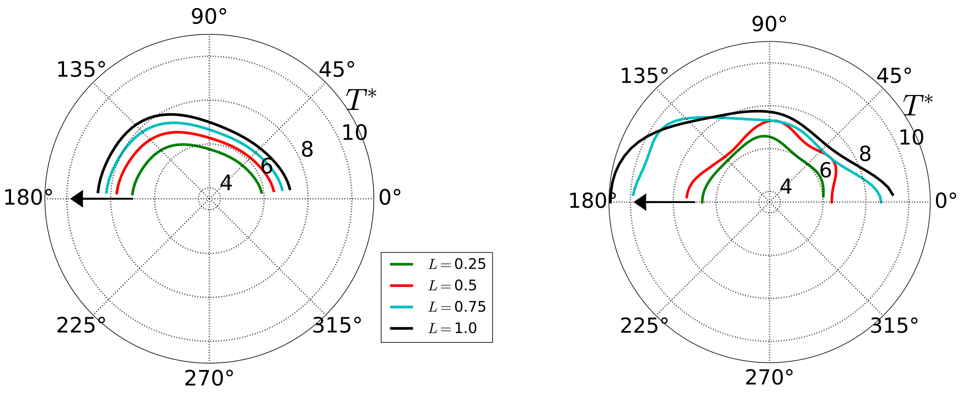

(a) (b)

Fig. 18: Circumferential variation of pin temperature for pin 1. The black arrow at 180° is oriented to the rod bundle center. (a) undamaged bundle (b) *Wheatsheaf* bundle

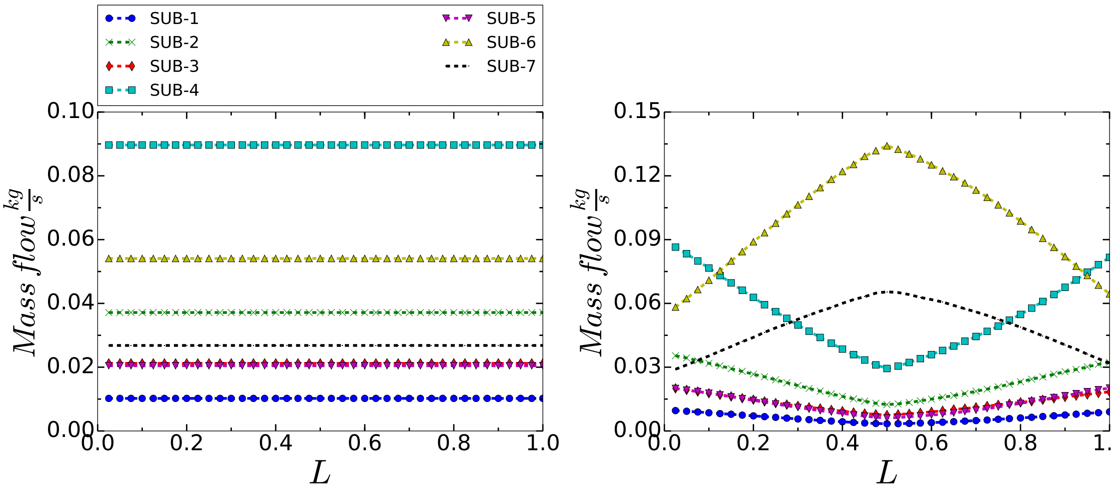

(a) (b)

Fig. 19: Mass flow variation within the full and partial subchannels present in the 30° sector. (a) undamaged bundle (b) *Wheatsheaf* bundle

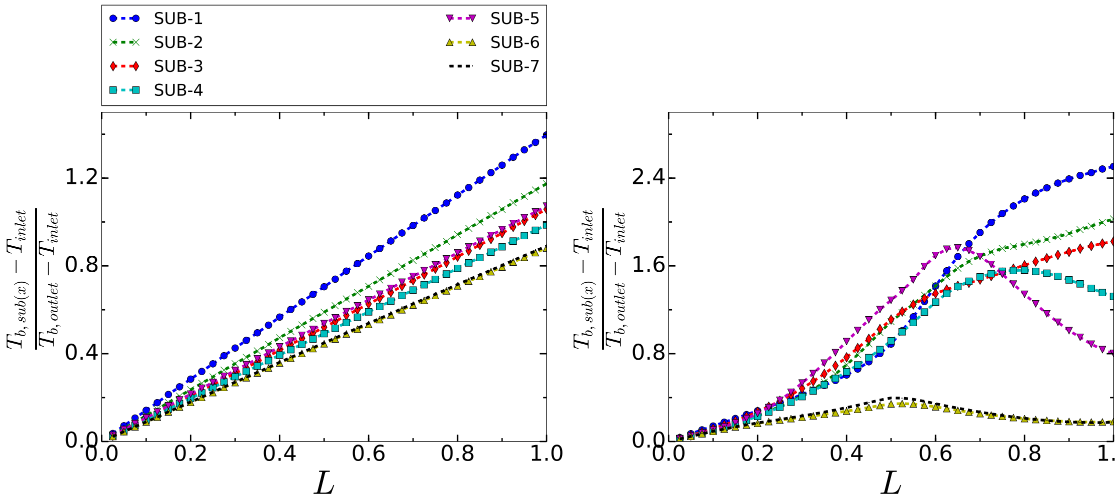

(a) (b)

Fig. 20: Axial fluid temperature variation within the full and partial subchannels present in the 30° sector. (a) undamaged bundle (b) *Wheatsheaf* bundle

with that obtained from EDF correlations, see Table 4, which shows good agreements. Correlations used are for the axial pressure loss in a rib-roughed AGR rod bundle[30].

Table 4: Pressure drop comparison

Reynolds number	Correlation (Pa)	Predicted (Pa)	% difference
60 000	109.072	109.67	0.551
100 000	304.40	305.99	0.522
150 000	687.50	690.04	0.369
200 000	1225.471	1228.10	0.214

It should be noted that AGR fuel pins have helicoidal ribs and adopting the wall function approach means that the induced swirl effects from the ribs is missed. Although this is the case, the approach does give an insight onto the effect of roughness.

The velocity profiles are shown in Fig.21. For Line_1, the reduction in peak axial velocity appears to be more significant than the smooth pin results obtained in the convergent section. This is evidenced by the profile at L=0.5 which has a much lower peak, of 0.75, in comparison to that of the smooth pin case. Imposing pin roughness appears to divert more flow from the interior, perhaps as a consequence of increased resistance. At L = 1.0 it is noted that the peak is ≈ 0.8, indicating the diverted flow is still yet to fully return. Similarly, for Line_2 at L = 0.5 the peak axial velocity is much lower in comparison to the smooth pin case. Furthermore at L = 1.0, there is a recovery in axial velocity. This again is in contrast to earlier presented results. It is also worth noting the asymmetries in the profiles identified earlier are not clearly evident in this plot. Fig.22 shows that the roughness case has much higher levels of k, which is to be expected. The temperature profiles across Line_1 in Fig. 23 shows a monotonic increase in temperatures. This is similar to smooth pin results, although the peak temperatures near the fuel pins are lower. The level of asymmetry evidenced for temperature in the smooth pin case is not replicated and, this is probably due to the increased mixing for this case. Line_2 shows a increase in temperature across the gap up until L = 1.0 where there is a decrease. In comparison smooth pins showed a monotonic temperature increase at this location. Finally to conclude peak temperature variation for fuel rod 1 is presented for the rough simulation in Fig. 24. It can be seen the location of peak can temperature occurs after the maximum distortion. This is similar to the smooth pin results, but in contrast the temperature levels on the wall are lower in comparison to those of the smooth pin case, as a result of increased heat transfer.

5. Conclusions

Flow and heat transfer in a damaged *Wheatsheaf* bundle have been investigated using the RANS method with the CFD software *Code_Saturne*. It is shown that the flow field within the damaged bundle significantly differs from that of an undamaged bundle. The coolant is diverted to regions of less resistance through the pin gaps. The distribution

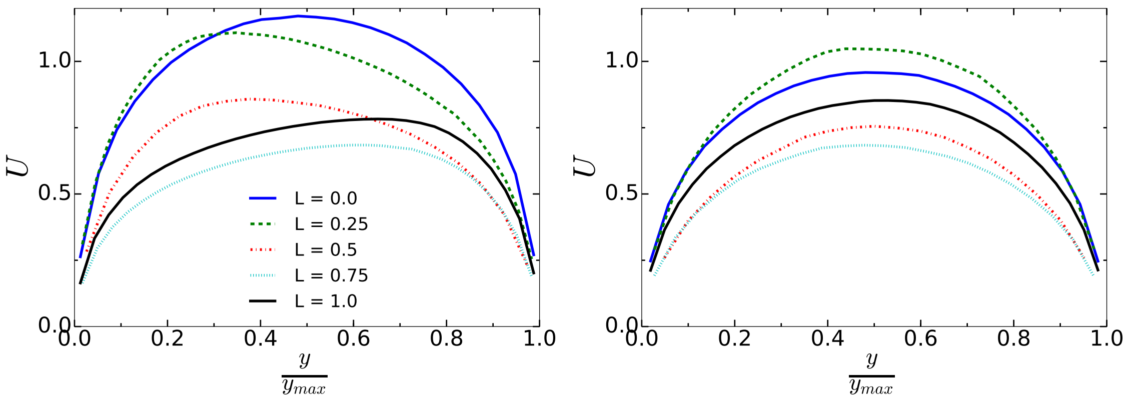

(a) (b)

Fig. 21: Profiles of normalised axial velocity for rough pins along (a) Line_1, (b) Line_2

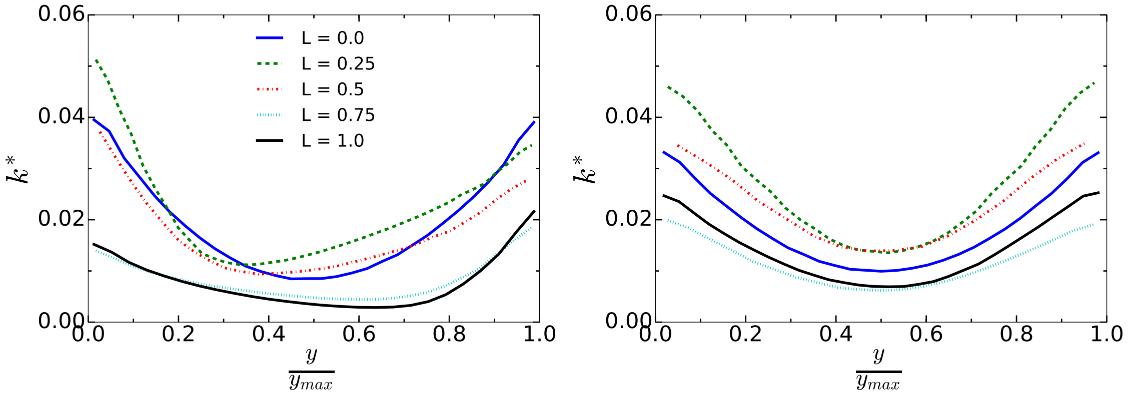

(a) (b)

Fig. 22: Profiles of normalised kinetic energy along (a) Line_1, (b) Line_2

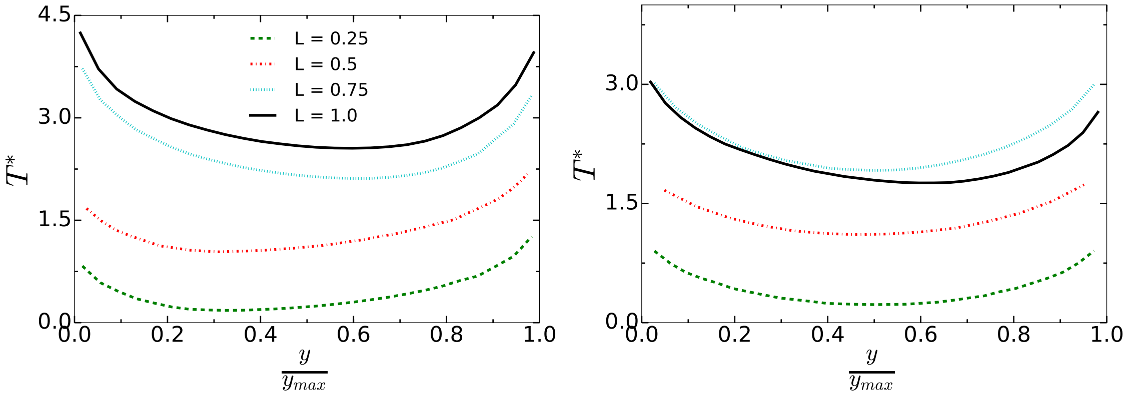

(a) (b)

Fig. 23: Profiles of normalised temperature along (a) Line_1, (b) Line_2

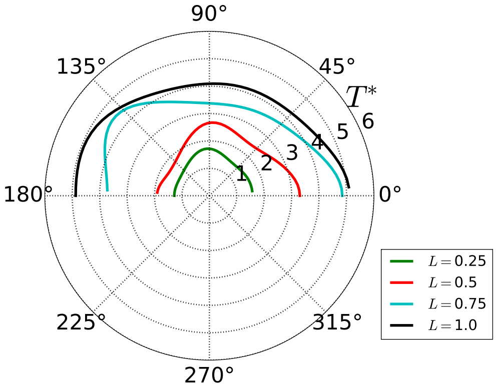

Fig. 24: Circumferential variation of pin temperature for pin 1. The black arrow at 180° is oriented to the rod bundle center

of mass flow rate in the subchannel at any height is largely proportional to the areas of the subchannels, but the velocity distribution is strongly influenced by the "history" - that is a strong delay is observed. In addition, the strong cross flow causes the formation of large flow circulations. Particle tracers demonstrate the flow is not only strongly three dimensional but also swirls around the fuel pins, resulting in unexpected can temperature distributions.

The peak can temperature at the worst damage section (half high) has been surprisingly found to be lower than that of the undamaged bundle at the same height, though stronger circumferential variation is observed. The peak can temperature increases strongly towards the top half of the damaged bundle though here the peak can temperature is higher than that of the intact fuel. In addition to the complex flow distribution which produces strongly nonuniform convection cooling effect, the bulk temperature of the subchannels shows large variations at any height, and vary non monotonically vertically, all of which contribute to the "abnormal" can distribution observed.

Acknowledgements

The work reported herein is sponsored through a studentship provided by EDF energy. The authors would like to thank the EDF R&D staff in Manchester, especially Mr. Jacopo De Amicis and Dr. Juan Uribe, for the technical support received.

References

[1] B. Ouma, S. Tavoularis, Flow measurements in rod bundle subchannels with varying rod-wall proximity, Journal of Nuclear Engineering and Design 131 (2) (1991) 193–208. doi:10.1016/0029-5493(91)90279-Q.

[2] F. Hofmann, Velocity and temperature distribution in turbulent flow in sodium cooled fuel elements with eccentric geometry, Nuclear Engineering and Design 14 (1) (1970) 43–50. doi:10.1016/0029-5493(70)90082-8.

[3] F. Heina, J; Chervenka, J; Mantlik, Results of local measurements of hydraulic characteristics in deformed pin bundle, Tech. Rep. UJV-4156-T, Rzez, Czech Republic (1977).

[4] A. Bogoslovskay, G. P. ; Cevolani, S ; Ninokata, H; Rinejski, A; Sorokin, A.P; Zhukov, LMFR core and heat exchanger thermohydraulic design: Former USSR and present Russian approaches, Tech. Rep. IAEA-TECDOC-1060, IAEA (1999).

[5] V. Kriventsev, H. Ninokata, Numerical method for simulation of fluid flow and heat transfer in geometrically disturbed rod bundles, Journal of Nuclear Science and Technology 37 (8) (2000) 646–653. doi:10.1080/18811248.2000.9714940.

[6] A. Davari, S. M. Mirvakili, E. Abedi, Three-dimensional analysis of flow blockage accident in

Tehran MTR research reactor core using CFD, Progress in Nuclear Energy 85 (2015) 605–612. doi:10.1016/j.pnucene.2015.08.008.

[7] A. Salama, S. E.-D. El-Morshedy, CFD simulation of flow blockage through a coolant channel of a typical material testing reactor core, Annals of Nuclear Energy 41 (2012) 26–39. doi:10.1016/j.anucene.2011.09.005.

[8] A. K. Chauhan, B. Prasad, B. Patnaik, Thermal hydraulics of rod bundles: The effect of eccentricity, Journal of Nuclear Engineering and Design 263 (2013) 218–240. doi:10.1016/j.nucengdes.2013.04.011.

[9] V. R. Skinner, A. R. Freeman, H. G. Lyall, Gas mixing in rod clusters, International Journal of Heat and Mass Transfer 12 (1968) 265–278. doi:10.1016/0017-9310(69)90010-6.

[10] J. D. Hooper, K. Rehme, Large-scale structural effects in developed turbulent flow through closely-spaced rod arrays, Journal of Fluid Mechanics 145 (-1) (1984) 305. doi:10.1017/S0022112084002949.

[11] T. Krauss, L. Meyer, Experimental investigation of turbulent transport of momentum and energy in a heated rod bundle, Journal of Nuclear Engineering and Design 180 (3) (1998) 185–206. doi:10.1016/S0029-5493(98)00158-7.

[12] B. H. Yan, Y. Q. Yu, H. Y. Gu, Y. H. Yang, L. Yu, Simulation of turbulent flow and heat transfer in channels between rod bundles, International Journal of Heat and Mass Transfer 47 (3) (2011) 343–349. doi:10.1007/s00231-010-0726-z.

[13] Y. Duan, S. He, Large eddy simulation of a buoyancy-aided flow in a non-uniform channel – Buoyancy effects on large flow structures, Nuclear Engineering and Design 312 (2017) 191–204. doi:10.1016/j.nucengdes.2016.05.007.

[14] M. M. Amin, Y. Duan, S. He, Large Eddy Simulation Study on Forced Convection Heat Transfer to Water at Supercritical Pressure in a Trapezoid Annulus, Journal of Nuclear Engineering and Radiation Science 4 (1) (2017) 14. doi:10.1115/1.4038161.

[15] D. Chang, S. Tavoularis, Numerical simulation of turbulent flow in a 37-rod bundle, Journal of Nuclear Engineering and Design 237 (6) (2007) 575–590. doi:10.1016/j.nucengdes.2006.08.001.

[16] D. Chang, S. Tavoularis, Unsteady Numerical Simulations of Turbulence and Coherent Structures in Axial Flow Near a Narrow Gap, Journal of Fluids Engineering 127 (3) (2005) 458. doi:10.1115/1.1900140.

[17] L. Meyer, From discovery to recognition of periodic large scale vortices in rod bundles as source of natural mixing between subchannels-A review, Nuclear Engineering and Design 240 (6) (2010) 1575–1588. doi:10.1016/j.nucengdes.2010.03.014.

[18] T. Sofu, T. H. Chun, W. K. In, Evaluation of Turbulence Models for Flow and Heat Transfer in Fuel Rod Bundle Geometries.

[19] A. C. Trupp, R. S. Azad, The structure of turbulent flow in triangular array rod bundles, Journal of Nuclear Engineering and Design 32 (1) (1975) 47–84. doi:10.1016/0029-5493(75)90090-4.

[20] W. Seale, Turbulent diffusion of heat between connected flow passages Part 1: Outline of problem and experimental investigation, Journal of Nuclear Engineering and Design 54 (2) (1979) 183–195. doi:10.1016/0029-5493(79)90166-3.

[21] C. W. Rapley, A. D. Gosman, The prediction of fully developed axial turbulent flow in rod bundles, Journal of Nuclear Engineering and Design 97 (3) (1986) 313–325. doi:10.1016/0029-5493(86)90167-6.

[22] V. Vonka, Measurement of secondary flow vortices in a rod bundle, Journal of Nuclear Engineering and Design 106 (2) (1988) 191–207. doi:10.1016/0029-5493(88)90277-4.

[23] P. Carajilescov, N. E. Todreas, Experimental and analytical study of axial turbulent flows in an interior subchannels of a bare rod bundle, Journal of Heat Transfer 98 (2) (1976) 262–268.

[24] K. Rehme, The structure of turbulence in rod bundles and the implications on natural mixing between

the subchannels, International Journal of Heat and Mass Transfer 35 (2) (1992) 567–581. doi:10.1016/0017-9310(92)90291-Y.

[25] B. Launder, D. Spalding, The numerical computation of turbulent flows, Computer Methods in Applied Mechanics and Engineering 3 (2) (1974) 269–289. arXiv:1204.1280v1, doi:10.1016/0045-7825(74)90029-2.

[26] F. Menter, Zonal Two Equation k-w Turbulence Models For Aerodynamic Flows, American Institute of Aeronautics and Astronauticsdoi:doi:10.2514/6.1993-2906.

[27] EDF, Code Saturne documentation Code Saturne 4.0.0 Theory Guide, Tech. rep., EDF (2013).

[28] T. B. Gatski, C. G. Speziale, On explicit algebraic stress models for complex turbulent flows, Journal of Fluid Mechanics 254 59–78.

[29] S. He, The Effect of Stringer and Channel Bow on Brick Temperature, Tech. rep., EDF Energy (2000).

[30] E. Romero, Cooling of Dropped AGR Fuel Elements - Specification of correlations for buoyancy free heat transfer and flow losses - axial flows, Tech. rep. (1994).